

Numerical estimation of densities

Y. Ascasibar^{1,2*} and J. Binney¹

¹*Theoretical Physics, 1Keble Road, Oxford OX1 3NP*

²*Harvard-Smithsonian Center for Astrophysics, 60 Garden St., Cambridge, MA02138, USA*

18 July 2018

ABSTRACT

We present a novel technique, dubbed FIESTAS, to estimate the underlying density field from a discrete set of sample points in an arbitrary multidimensional space. FIESTAS assigns a volume to each point by means of a binary tree. Density is then computed by integrating over an adaptive kernel.

As a first test, we construct several Monte Carlo realizations of a Hernquist profile and recover the particle density in both real and phase space. At a given point, Poisson noise causes the unsmoothed estimates to fluctuate by a factor ~ 2 regardless of the number of particles. This spread can be reduced to about 1 dex (~ 26 per cent) by our smoothing procedure. The density range over which the estimates are unbiased widens as the particle number increases. Our tests show that real-space densities obtained with an SPH kernel are significantly more biased than those yielded by FIESTAS. In phase space, about ten times more particles are required in order to achieve a similar accuracy.

As a second application we have estimated phase-space densities in a dark matter halo from a cosmological simulation. We confirm the results of Arad et al. (2004) that the highest values of f are all associated with substructure rather than the main halo, and that the volume function $v(f) \sim f^{-2.5}$ over about four orders of magnitude in f . We show that a modified version of the toy model proposed by Arad et al. explains this result and suggests that the departures of $v(f)$ from power-law form are not mere numerical artefacts. We conclude that our algorithm accurately measure the phase-space density up to the limit where discreteness effects render the simulation itself unreliable. Computationally, FIESTAS is orders of magnitude faster than the method based on Delaunay tessellation that Arad et al. employed, making it practicable to recover smoothed density estimates for sets of 10^9 points in 6 dimensions.

Key words: methods: data analysis – methods: numerical – dark matter – galaxies: haloes – galaxies: kinematics and dynamics

1 INTRODUCTION

The estimation of a continuous density field from a set of discrete sample points is a common problem. For example, the estimation of the matter density in real space is fundamental in numerical studies of cosmic structure formation, and lies at the heart of N-body codes that solve the Poisson equation, such as ART (Kravtsov et al. 1997) or MLAPM (Knebe et al. 2001). It also plays an important rôle in hydrodynamic codes based on Smooth Particle Hydrodynamics (SPH) (see e.g. Monaghan 1992; Springel & Hernquist 2002, and references therein).

Several problems of current interest involve the estimation of the density of points in phase space (e.g., Binney 2004; Arad et al. 2004). Although violent relaxation and

phase-mixing tend to disrupt substructures, both stars and dark matter may retain information about their initial conditions for a relatively long time. In principle, it would be possible to trace the merging history of our galaxy by looking for phase-space streams in the stellar population (see e.g. Helmi & White 1999). These streams might be identified as regions of enhanced density in either real space, phase space, or integral space (Helmi et al. 2003).

Most algorithms for estimating densities require the imposition of a metric on the space occupied by sample points – that is, they assume that the ‘distance’ between every two points is defined. However, often the underlying physical problem does not have any metric. In such a case, a metric can be imposed by specifying a matrix K_{ij} that relates one unit along the i -th axis to one unit on the j -th axis. For example, in the case of phase space, we need a dimensional constant K to relate positions and velocities,

* E-mail: yago@thphys.ox.ac.uk

so that a velocity difference v is equivalent to a spatial offset of Kv . The local velocity dispersion σ would thus define a length scale $K\sigma$ that will in general bear no relation to the actual length scale l . For example, in a singular isothermal sphere, $l \propto r$ while $K\sigma$ is constant. This effect will be present in many applications, amongst them the estimation of phase-space densities within dark matter haloes.

In this paper we present an algorithm for density estimation that does not require a metric. We show that our method provides fast and accurate estimates of both real-space and phase-space densities. The algorithm's independence of the existence of a metric makes it applicable to a wide class of problems in statistics (see e.g. Silverman 1986, for a review), in which one wishes to find clusters of data points in a space in which different axes represent quantities with different physical dimensions. For example, a data point could be composed of a position, a redshift and luminosities in several bands, and one wishes to find groupings of physically related points. Some automated classification algorithms based on probability densities are currently being applied to large galaxy surveys (e.g. Richards et al. 2004) that could tremendously benefit from the possibility of working in a completely arbitrary space.

When a metric is available for the sample space, estimators based on kernels are widely used. For example, in SPH (Lucy 1977; Gingold & Monaghan 1977) one obtains the density from

$$\hat{\rho}_{\text{SPH}}(\mathbf{r}) = \sum_{p=1}^N m_p W(\mathbf{r} - \mathbf{r}_p, h), \quad (1)$$

where m_p is the mass of each particle, \mathbf{r}_p its position, and $W(\mathbf{r}, h)$ is a kernel characterized by a smoothing scale, h . Adaptive resolution is achieved by setting h to the distance to the N_n -th nearest neighbour (Hernquist & Katz 1989).

A promising alternative to equation (1), Voronoi tessellations (see e.g. Okabe et al. 1992) have been used in astrophysics to identify overdensities in a Poissonian distribution of X-ray photons (Ebeling & Wiedenmann 1993), as well as detecting galaxy clusters in observational surveys (e.g. Ramella et al. 2001; Kim et al. 2002; Marinoni et al. 2002). Similar in spirit, the Delaunay Tessellation Field Estimator (DTFE, Pelupessy et al. 2003, and references therein) estimates the densities of a set of points from the volume of the Delaunay cells they belong to. A continuous field can be obtained by linear interpolation (Bernardeau & van de Weygaert 1996). Arad et al. (2004) have recently applied the DTFE method to the estimation of six-dimensional phase-space densities in N-body experiments. They find that the volume distribution function, $v(f)$, for relaxed haloes follows a power law over more than 4 decades in f . For high values of the phase-space density, $v(f)$ is dominated by ‘cold’ substructure rather than by the parent halo.

However, the definition of distance underlying a Voronoi or Delaunay tessellation is not at all obvious in phase space. The chosen metric determines which particles are close neighbours, and thus the resulting tessellation and the densities that are assigned to each particle. The impact of such an ad-hoc choice is extremely difficult to quantify, and it would require a problem-by-problem study. It is easy to understand, though, that one's choice may be of crucial impor-

tance in the general case, in which very different scales (e.g. a halo with substructure) or obviously non-Euclidean spaces (e.g. number density of star-forming galaxies per stereoradian per redshift per morphological type per luminosity) are involved. On the other hand, we would like the results to be as stable as possible if we decided to work in different units (e.g. comoving distance instead of redshift, or absolute magnitude instead of luminosity). No linear scaling K_{ij} could accommodate such a transformation. The choice of units and coordinate types (e.g. radial, polar, logarithmic) is critical in metric-based schemes.

We present here a non-metric Field Estimator for Arbitrary Spaces (FIESTAS), thoroughly described in Section 2. Tests of the algorithm are presented in Section 3, where we attempt to recover both the real- and phase-space density from random realizations of a Hernquist (1990) profile, for which an analytical distribution function is known. We investigate the phase-space structure of a realistic dark matter halo from an N-body simulation in Section 4, and discuss the computational performance of our method in Section 5. Section 6 summarizes our main conclusions.

2 THE ALGORITHM

2.1 Tessellation

Like the DTFE method, FIESTAS is based on a tessellation of the d -dimensional space, i.e. a division of R^d in into mutually disjoint polygons. However, we do not resort to a Delaunay or Voronoi tessellation. Although these can adapt very efficiently to the geometry of the problem, they require a metric to define distances. Moreover, they become computationally expensive for large datasets, particularly when d is large.

Instead, we use a binary tree to tessellate our hypervolume by means of a recursive procedure. Given a set of N points, we split the space along the i -th coordinate. In the ideal case, one would classify the points according to their position relative to the median x_i , thus obtaining two partitions with $N/2$ points each. In practice, we select the two closest points (one from each side) to the mean $\langle x_i \rangle$ and split the i -th axis at $x_{\text{split}} = (x_+ + x_-)/2$. This is sufficiently accurate for our purposes, and much more efficient than computing the median.

The process is repeated for both subsets until the initial space is divided in N hyper-boxes, each containing a single point. A first estimate of the local density is just the weight of the point, which we shall call its mass m_p , divided by the volume of its hyper-box,

$$\hat{\rho}_p = \frac{m_p}{\hat{V}_p}. \quad (2)$$

The construction of a two-dimensional binary tree is illustrated in Fig. 1. In the general case, the order in which the coordinates are selected for splitting should be chosen at random. Nevertheless, we try to respect the symmetries of our particular problem (the estimation of phase-space densities) as much as possible, so we alternately split a real-space and a velocity-space coordinate. In both cases, we always select the axis with the highest elongation, $\langle x_i^2 \rangle - \langle x_i \rangle^2$. Proceeding in this way does not significantly affect the estimated densities, but it alleviates numerical problems that

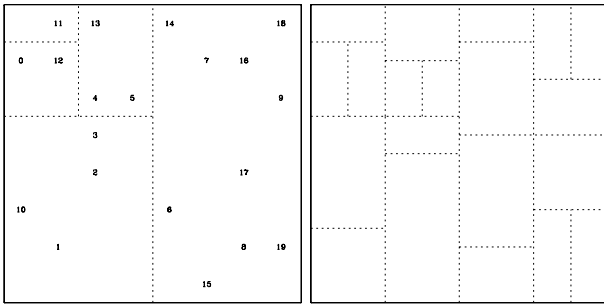


Figure 1. Construction of a two-dimensional binary tree. The first division occurs along the horizontal axis, and x_{split} is set between points 5 and 14. The left part is then divided along the vertical axis (between points 5 and 3), and so on.

arise when two points have very similar (or equal) values of a coordinate x_i . It also yields cells that are more or less cubic when projected onto the position or velocity sub-spaces, which both have Euclidean metrics. However, we do not impose any relation between these sub-spaces, nor do we attempt to compute any ‘distance’ involving more than one coordinate at a time.

As discussed above, Voronoi or Delaunay tessellations are not well defined in spaces lacking a metric. Our scheme is not sensitive to the particular choice of units, the characteristic scale (if any) or the nature of each dimension, although the precise shape of our orthohedral cells depends on the choice of principal axes (for those sub-spaces admitting rotations) as well as on the splitting sequence. None the less, the uncertainty due to this non-uniqueness is comparable to or lower than the intrinsic Poisson noise of the point distribution.

2.2 Boundary effects

A problem common to all tessellations (with Delaunay triangulation probably yielding the smallest errors) is the choice of a boundary for the system. Since the density field can be completely arbitrary, there is no reason to expect that the point distribution under study should fit into an orthohedral bounding box.

In particular, there is no warranty that the field will be well sampled near the boundaries. This is clearly seen, for example, if we take a finite distribution, fully contained within the bounding hyper-box, and enlarge the box without altering the data points themselves. Most algorithms, including ours, will be stable in the innermost regions, where every point is surrounded by neighbours (i.e. the field is well sampled), but densities in the outskirts will be lower because each point would be associated with a larger volume. This phenomenon is not an issue when we are interested in a small subset of the point distribution or when periodic boundary conditions apply. Then, boundary effects are hidden within the Poisson noise. However, we expect to encounter this difficulty fairly often, since it arises in any distribution sampling an infinite space, specially when there is a sharp density gradient in the outermost regions. In the estimation of phase-space densities, it manifests most acutely for particles in the tails of the velocity distribution.

We try to compensate this effect by redefining the

boundary of the system. Consider, for example, a sample point that lies at \mathbf{x}^p within a box that extends to the current boundary of the sampled region, in a portion of the hyperplane $x_i = X_{\text{max}}$. Let the opposite (interior) face of the point’s volume be defined by the hyperplane $x_i = X_{\text{min}}$. Then we bring the outer face of the box from X_{max} into the hyperplane $x_i = x_i^p + (x_i^p - X_{\text{min}})$. This redefinition of the outer face of the box reduces its volume and thus increases the derived density. The changes are small if the field is well sampled near the boundaries, because then the point will be, on average, in the middle of the original box. If the field is severely undersampled, x_i^p will lie much nearer to X_{min} than X_{max} and the change will be more significant. The correction is a crude attempt to adapt the shape of the boundary of the volume within which densities are determined to the region of space that is usefully sampled.

2.3 Smoothing

The prescription outlined above provides a very fast estimation of the density. It has the additional advantage that volume integrals of the type

$$I = \int_V \Psi[\rho(\mathbf{x})] d^d \mathbf{x} \quad (3)$$

are readily computed as

$$\hat{I} = \sum_{p=1}^N \Psi(\hat{\rho}_p) \times (\hat{V}_p \cap V). \quad (4)$$

However, the estimator (2) is prone to a large statistical error. Even worse, the associated uncertainty does not vanish, no matter how many points we use. As noted by Arad et al. (2004), the probability distribution $p(\hat{\rho}/\rho)$ does not approach a Dirac delta function, even in the limit $N \rightarrow \infty$. This problem is common to all methods based on a fixed number of points (in our case, just one). At constant density, increasing the total number of points yields smaller and smaller volumes. Since the process is scale-invariant, both the probability distribution $p(\hat{\rho}/\rho)$ and the relative error $\Delta\hat{\rho}/\rho$ remain constant.

Ideally one has just enough particles that the density changes by only a small amount between neighbouring particles. Increasing the resolution beyond this ideal does not of itself reduce the error in the measured density, but it does make it possible to reduce the statistical error by *smoothing* our density estimate (2). FIESTAS implements a kernel interpolation, similar in spirit to the SPH scheme. For a given point \mathbf{x} in d -dimensional space, we integrate the mass over a region V around \mathbf{x} . First, the mass of each data point is uniformly distributed within its assigned volume, \hat{V}_p . Then, using equation (4) we calculate

$$\hat{M}(\mathbf{x}, V) = \sum_{p=1}^N \hat{\rho}_p \times (\hat{V}_p \cap V), \quad (5)$$

and we set

$$\hat{\rho}(\mathbf{x}, V) = \frac{\hat{M}(\mathbf{x}, V)}{V} \quad (6)$$

The shape of V is chosen to be orthohedral, both because of computational efficiency and because we do not assume the

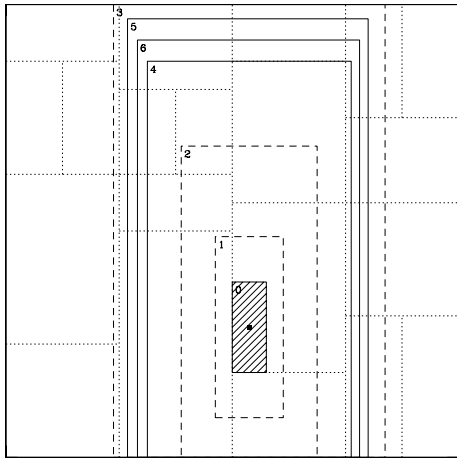


Figure 2. Smoothing around the position of point 6 in Fig. 1. We start with the shadowed box, defined by the nearest faces of the cell. We double the box size (dashed lines) until $\hat{M} > M_k$, and then find the exact solution (thick solid line) by repeatedly halving the search interval (thin solid lines). Numbers at the top left corner of each box illustrate this sequence.

existence of a metric for the space¹. We adjust the volume V as described below such that $\hat{M}(\mathbf{x}, V) = M_k$, where the *kernel mass* M_k is the only free parameter in FIESTAS. Basing on our preliminary tests, we suggest $M_k \simeq 10m_p$ as a compromise between accuracy and spatial resolution.

The boundaries of the volume V are the hyperplanes on which the i -th coordinate equals $x_i \pm \Delta x_i$, where the half-width Δx_i is determined iteratively (see Fig. 2). We start with Δx_i equal to the minimum distance along the i -th axis to an edge of the hyper-box containing \mathbf{x} . With this prescription, $\hat{M} \leq m_p$. We then double all the Δx_i until $\hat{M} > M_k$, and then find the exact value by repeatedly halving the search interval.

3 HERNQUIST PROFILE

In order to test our algorithm, random realizations of a Hernquist (1990) profile have been generated with different numbers of particles, N . We then try to reconstruct the density field both in real and phase space, assessing the accuracy of our estimation, as well as the importance of smoothing and correcting for boundary effects.

The density in real space is given by

$$\rho(r) = \frac{M}{2\pi a^3} \frac{1}{r/a(1+r/a)^3}, \quad (7)$$

which leads to a cumulative mass

$$M(r) = M \left(\frac{r/a}{1+r/a} \right)^2 \quad (8)$$

and a gravitational potential

$$\Phi(r) = -\frac{GM}{a} \frac{1}{1+r/a}. \quad (9)$$

¹ It would be hard to define any other shape (e.g. a hyper-sphere) without specifying a metric.

The main advantage of the Hernquist profile, which greatly simplifies our analysis, is that the phase-space density can be evaluated analytically as a function of energy,

$$f(E) = \frac{M/a^3}{4\pi^3(2GM/a)^{3/2}} \times \frac{3 \sin^{-1} q + q\sqrt{1-q^2}(1-2q^2)(8q^4-8q^2-3)}{(1-q^2)^{5/2}}, \quad (10)$$

where M is the total mass, a is a scale length and

$$q \equiv \sqrt{-\frac{E}{GM/a}}. \quad (11)$$

The Hernquist (1990) model has been widely used to model the mass distribution of dark matter haloes in numerical simulations, and it provides a good fit to the observed surface brightness of bulges and elliptical galaxies. Some other profiles have been proposed in the literature (e.g. Navarro et al. 1997; Moore et al. 1999) that better fit the results of cosmological N-body simulations, but they lack an analytical expression for the phase-space density.

The actual generation of random N-body realisations is fairly straightforward once the mass profile and the phase-space density are known. The radial coordinate is chosen by generating a random number x between 0 and 1, and then inverting equation (8),

$$\frac{r}{a} = \frac{\sqrt{x}}{1-\sqrt{x}}. \quad (12)$$

Then, velocities are assigned from the distribution

$$p(v) dv = \frac{4\pi}{\rho(r)} f(v^2/2 + \Phi(r)) v^2 dv \quad (13)$$

using von Neumann rejection (see e.g. Press et al. 1992). We generate a tentative velocity v , uniformly distributed between 0 and $v_{\max} = \sqrt{-2\Phi(r)}$, and an auxiliary random number x between 0 and $v_{\max}^2 f(v_{\max})$. The velocity is accepted only if $x < v^2 f(v)$. Otherwise, two new random numbers are generated for v and x until a value is finally accepted. Angular coordinates for both positions and velocities are obtained from the variables $0 < \phi < 2\pi$ and $-1 < \cos \theta < 1$.

3.1 Real space

The real-space density obtained from two random realizations with $N = 100$ and $N = 10^5$ particles is compared in Fig. 3 with the theoretical profile (7). We corrected for boundary effects and applied smoothing with $M_k = 10m_p$ in both cases. The mean density and standard its deviation were computed in 30 logarithmic bins, subject to the constraint that each bin should contain at least 2 particles. For $N = 100$, the profile is accurately recovered for about one decade in radius. In the central regions, lack of resolution erases the density cusp, while in the outskirts of the system, the sampling provided by 100 points is too coarse for a reliable reconstruction of the density field.

This can be more clearly seen in Fig. 4, where we plot the ratio $\hat{\rho}/\rho$ with respect to the theoretical density ρ for different values of N . In all cases, the estimated density is most reliable in the intermediate range. There is some inner radius r_{\min} , set by the number of particles, beyond which

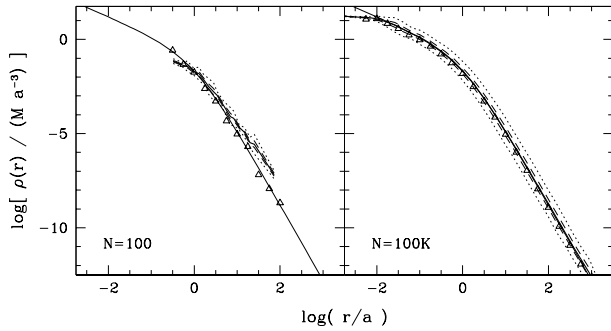


Figure 3. Reconstruction of a Hernquist density profile from two random realizations with $N = 100$ (left) and $N = 10^5$ (right) particles. Thin solid lines show equation (7). The average estimation given by FiESTAS is plotted as a thick solid line. Dashed and dotted lines represent one and three-sigma scatter, respectively. The density profile derived from particle counts in logarithmic radial bins is shown as open triangles.

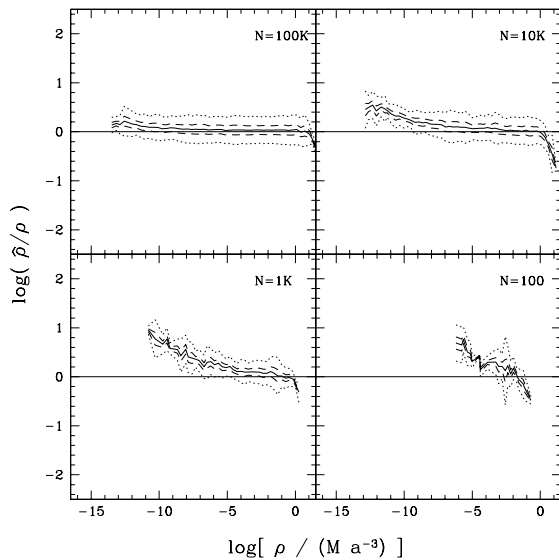


Figure 4. Systematic dependence of $\hat{\rho}/\rho$ on ρ for different numbers of particles in a Hernquist sphere. Boundary correction and smoothing have been applied in all cases. Line styles are the same as in Fig. 3.

we are not able to resolve the cusp. On the other hand, there is some outer radius r_{\max} , also set by N , where the density becomes so low that there are simply not enough points to sample the field, and the estimate $\hat{\rho}$ is dominated by boundary effects.

Fig. 5 shows that the boundary correction is relevant for the unsmoothed estimator (bottom panels) at low densities, but it has a weaker effect on the smoothed estimate (top panels). For particles at the boundary, the volume assigned by the binary tree is usually too large, because the bounding box is a cuboid, whereas the density field has spherical symmetry. There is a lot of empty space from the last particle to the appropriate faces of the bounding box, resulting in an artificially large value of V_p . The density given by expression (2) is thus severely underestimated for these particles. When the smoothed estimator (6) is used instead, the effect is more limited, since each particle will typically be surrounded by

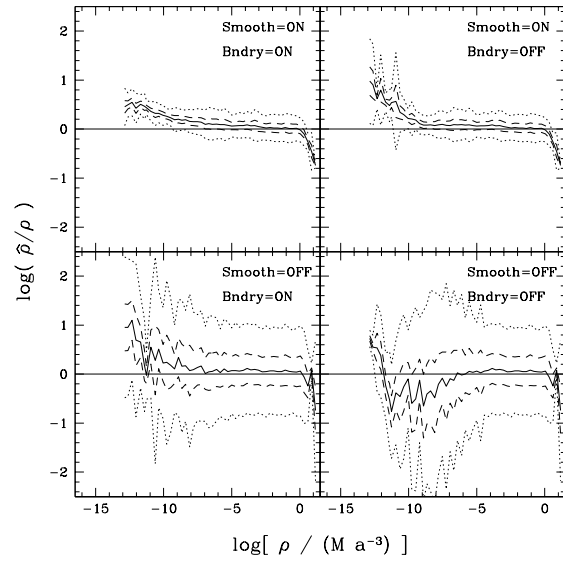


Figure 5. Systematic dependence of $\hat{\rho}/\rho$ on ρ for different prescriptions. Density has been smoothed on the top panels. Left panels apply the boundary correction. All plots correspond to a realization of a Hernquist sphere with $N = 10^4$ particles. Line styles are the same as in Fig. 3.

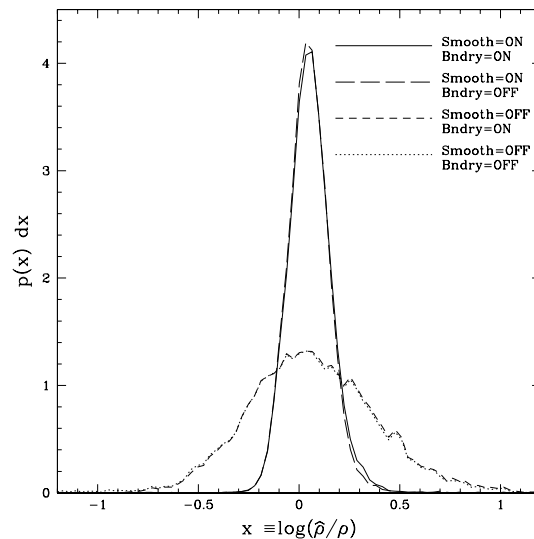


Figure 6. Probability distribution $p(\hat{\rho}/\rho)$ for a Hernquist sphere with $N = 10^4$ particles, using different prescriptions. Correction for boundary effects is negligible, while smoothing considerably reduces the uncertainty.

higher density neighbours. These will dominate the volume integral, minimising the contamination from artificially low-density particles.

Moreover, the number of particles affected by the boundary correction constitutes a relatively small fraction of the total. As can be seen in Fig. 6, the overall distribution of $\hat{\rho}/\rho$ is not altered at all by considering boundary effects, even for moderate resolutions ($N = 10^4$ particles). This correction becomes more important for very poor resolutions, or in higher-dimensionality spaces, in which the fraction of data points at the boundary is substantially larger.

As previously mentioned, the probability distribution

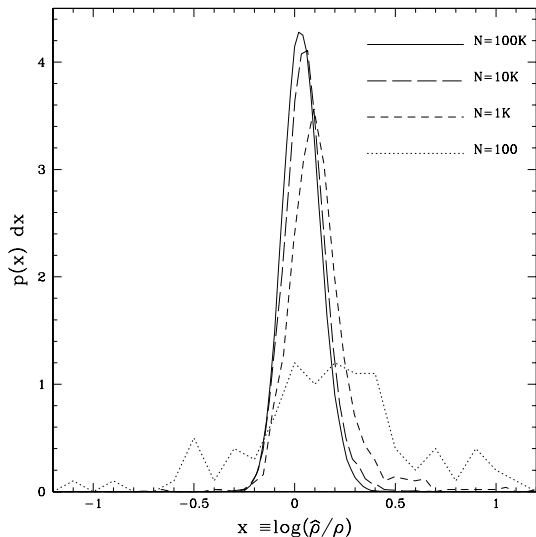


Figure 7. Probability distribution $p(\hat{\rho}/\rho)$ for different numbers of particles in the Hernquist sphere. The distribution is broader and more skewed as N decreases.

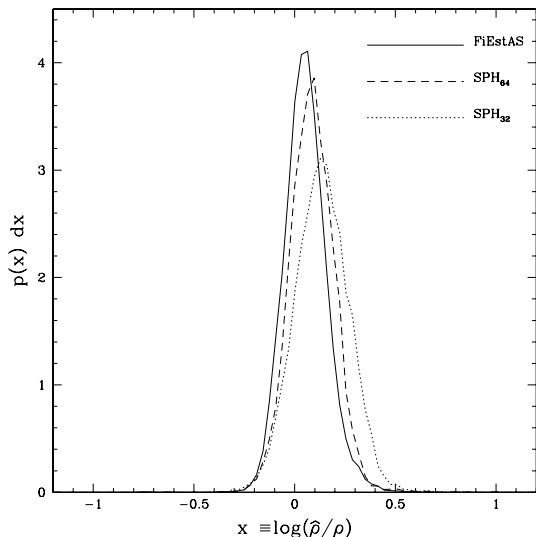


Figure 8. Comparison between FiEstAS (with $Mk = 10$) and SPH (using 32 and 64 neighbours) for a Hernquist sphere with $N = 10^4$ particles.

$p(\hat{\rho}/\rho)$ does not tend to a Dirac delta function as $N \rightarrow \infty$ (see Fig. 7). If our point distribution is locally Poissonian, the dispersion can be reduced by averaging over a neighbouring volume containing more particles. The underlying density field must be approximately constant (i.e. we must have enough resolution) over the smoothing region. This assumption breaks down at the very centre, as well as in the outermost parts. In these regions, smoothing may even worsen the density estimate, but for most particles, it yields a significant improvement in accuracy (see Figs 5 and 6).

It is encouraging that $p(\hat{\rho}/\rho)$ varies very little for $N > 10^3$ particles, suggesting that it has converged to its asymptotic form. Our $p(\hat{\rho}/\rho)$ is well modelled by a log-normal distribution with $\langle \log(\hat{\rho}/\rho) \rangle \leq 0.04$ dex and $\sigma \leq 0.1$ dex, which corresponds to a relative error $\Delta\rho/\rho$ smaller than 26 per cent.

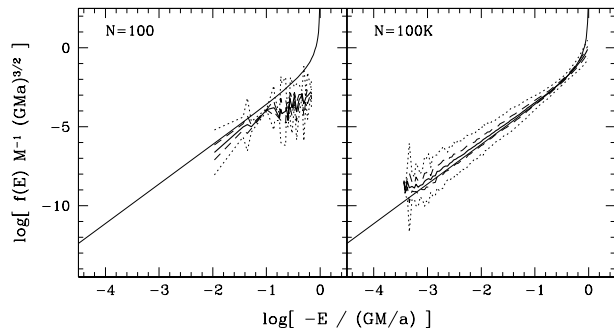


Figure 9. Phase-space density of two random realizations of a Hernquist model, with $N = 100$ (left) and $N = 10^5$ (right) particles. Line styles are the same as in Fig. 3. Thin solid lines represent equation (10).

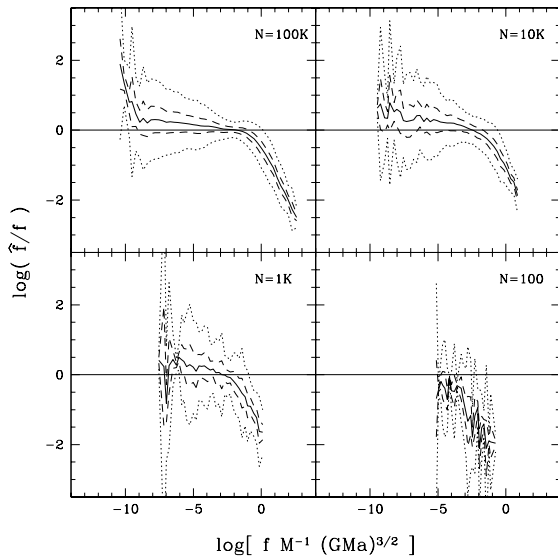


Figure 10. Dependence of \hat{f}/f on f for a Hernquist model sampled with various N . Smoothing and boundary corrections are both on.

In Fig. 8 FiEstAS is compared with the popular SPH method. We set the smoothing length in the latter using 32 and 64 neighbours. FiEstAS gives a slightly more accurate (i.e. lower scatter) estimate, and the results are significantly less biased towards large $\hat{\rho}/\rho$. In order to obtain similar results, the SPH method would require averaging over more than 64 neighbouring particles, which is considerably demanding from the computational point of view, and seriously degrades the spatial resolution of the estimator.

3.2 Phase space

In this section, we test the performance of our algorithm in six-dimensional phase space. From the distribution function (10) we can randomly sample the phase space with any number N of particles. Fig. 9 shows the results for two realizations of a Hernquist model with different values of N . For $N = 100$, we are barely able to recover the qualitative behaviour of the theoretical profile, while with $N = 10^5$ the points scatter around the analytic value over eight orders of magnitude in f .

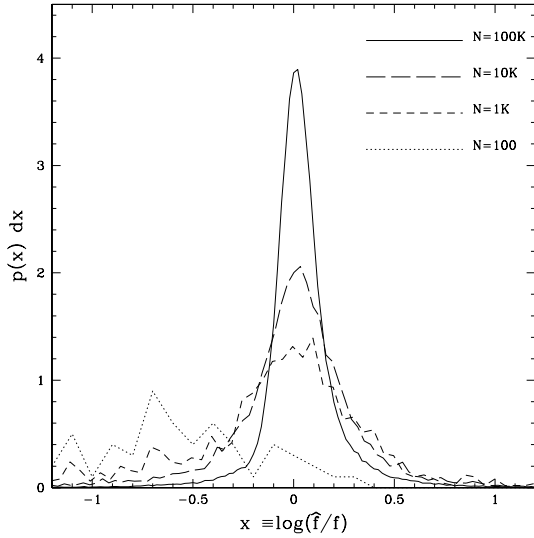


Figure 11. Probability distribution $p(\hat{f}/f)$ for a Hernquist model sampled with various N . Smoothing and boundary corrections are both on.

The effect of increasing the number of particles can be appreciated in Fig. 10. More resolution extends the range of phase-space densities that are accurately estimated. As in the real-space case, lack of resolution leads to systematic underestimation of the highest densities, while there is a tendency to overestimate the lowest densities. Fig. 11 shows that with $N = 10^4$ the probability distribution $p(\hat{f}/f)$ is reasonably unbiased, $\langle \log(\hat{f}/f) \rangle \leq 0.04$ dex, and has a typical spread $\sigma \sim 0.1$ dex comparable to that in real space. Note however that more resolution is obviously needed in order to assess convergence. Comparison with the real-space densities shown in Figs. 3, 5 and 7 suggests that increasing the dimensionality of the space from 3 to 6 requires a factor of order 10 more points to achieve a similar distribution. In general, it seems reasonable to expect that the number of points needed to properly sample a given space increases exponentially with the number of dimensions d in a way similar to the typical number of neighbours, roughly 2^d .

We quantify in Fig. 12 the importance of smoothing and boundary corrections. In six dimensions, a very large fraction of particles lie close to at least one of the 12 faces of the bounding hyper-box. The correction for boundary effects is thus relevant even for $N = 10^4$. Using the smoothed estimator considerably reduces the dispersion in $\log(\hat{f}/f)$, but \hat{f} is still biased low when boundary effects are not accounted for. There are so many particles whose initial density (2) was underestimated that they make a significant contribution to the volume integral in (6).

Another effect of the coarser sampling in six dimensions is that the softening of the cusp is more noticeable than in the three-dimensional case. Note also that the slope of the phase-space density for $E \rightarrow 0$ is much steeper than the physical density at low r , which makes it difficult to sample the high- f region adequately.

None the less, the smoothed estimator (6) greatly reduces the spread in \hat{f}/f . As can be seen in Fig. 13, the unsmoothed estimator yields a dispersion of about one decade around the true value of f , regardless of whether the boundary effects have been corrected or not. Such a large disper-

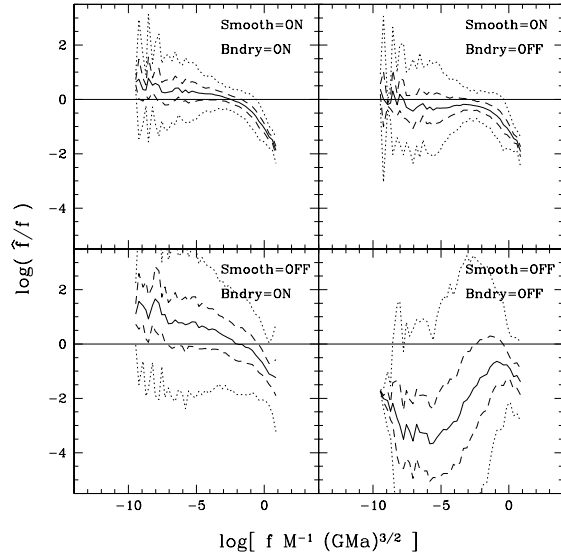


Figure 12. Dependence of \hat{f}/f on f for a Hernquist model of $N = 10^4$ particles when various combinations of smoothing and boundary correction are used.

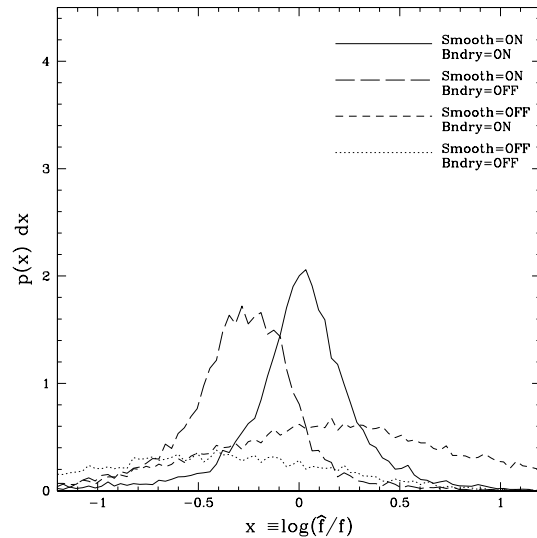


Figure 13. Probability distribution $p(\hat{f}/f)$ for a Hernquist model of $N = 10^4$ particles when various combinations of smoothing and boundary correction are used.

sion coincides approximately with the statistical error reported by Arad et al. (2004).

Arad et al. investigated the volume distribution function

$$v(f_0) = \int \delta[f(\mathbf{x}, \mathbf{v}) - f_0] d^3\mathbf{x} d^3\mathbf{v}, \quad (14)$$

which gives the volume of phase space in which f lies in the interval $(f_0, f_0 + df)$, i.e. $dV = v(f) df$. Since the mass contained in particles that have phase space densities within df of f is

$$\frac{dm}{df} = fv(f), \quad (15)$$

we can estimate $v(f)$ from dm/df . We obtain the latter by

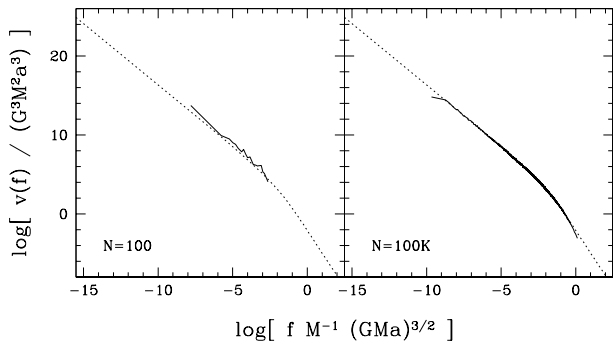


Figure 14. Volume distribution $v(\hat{f})$ for Hernquist models with $N = 100$ and $N = 10^5$. The analytic result (17) is plotted as a dotted line.

sorting the particles in order of increasing \hat{f} -values and then binning them. In our tests the bins contain 50 particles each, except in the case $N = 100$, when we take only 5 particles per bin.

Arad et al. (2004) show that errors in \hat{f} cause the estimated volume function $\hat{v}(f)$ to be the convolution

$$\hat{v}(f_0) = \int_0^\infty v(f) p(f_0/f) f^{-1} df. \quad (16)$$

For $v(f) \propto f^{-\alpha}$, we find that $\hat{v}(f_0) \propto f_0^{-\alpha}$, where the constant of proportionality is an integral that is independent of f_0 . From this result it follows that when $v(f)$ is well approximated locally by a power law over the range in which $p(f/f_0)$ is non-negligible, the measured logarithmic slope of $\hat{v}(f)$ at f_0 will equal the logarithmic slope of the underlying function $v(f)$.

When f is a function $f(E)$ of energy alone, we obtain the theoretical volume distribution from

$$v[f(E)] = \frac{g(E)}{f'(E)}, \quad (17)$$

where $g(E)$ is the density of states and $f'(E)$ denotes the derivative of f with respect to E . For a Hernquist profile, f is given by equation (10), and the density of states is

$$g(E) = \frac{2\pi^2 a^3 (2GM/a)^{1/2}}{3q^5} [3(8q^4 - 4q^2 + 1) \cos^{-1} q - q(1 - q^2)^{1/2} (4q^2 - 1)(2q^2 + 3)]. \quad (18)$$

Fig. 14 demonstrates that it is possible to recover the qualitative behaviour of $v(f)$ even with a resolution as poor as $N = 100$. Deviations from the theoretical volume distribution are plotted in Fig. 15 for different numbers of particles. Results for $N \geq 1000$ stay within a factor of 2 of the true $v(f)$, although some systematic errors are present near the turnover of $f(E)$, where the distribution function cannot be described as a power law.

4 COSMOLOGICAL SIMULATION

Having assessed the accuracy of our algorithm, we apply it to a realistic case in which the phase-space structure is not known a priori. We select a $\sim 10^{14} M_\odot$ halo from an N-body simulation accomplished with the publicly-available code GADGET (Springel et al. 2001; Springel & Hernquist

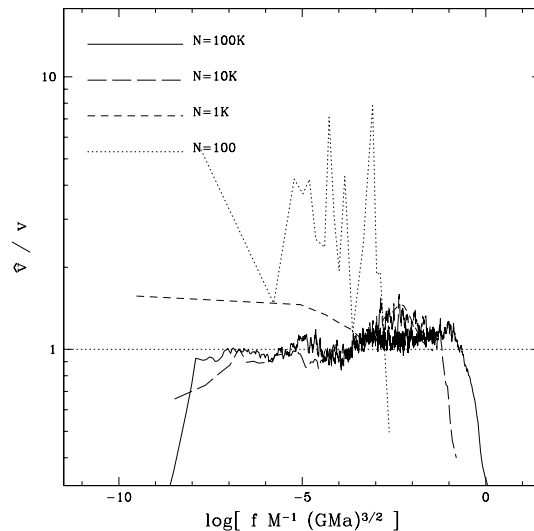


Figure 15. Systematic dependence of \hat{v}/v on f for Hernquist models with various N .

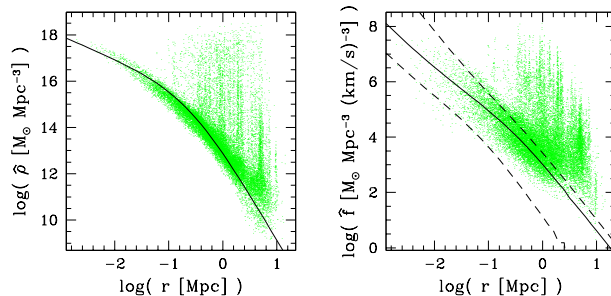


Figure 16. Density profile, both in real (left) and phase (right) space, of a $10^{14} M_\odot$ halo in a numerical simulation ($N \sim 10^6$). Solid lines show a Hernquist model with $M = 3.6 \times 10^{14} M_\odot$ and $a = 250$ kpc. In phase space, $v^2 = 3\sigma_r^2$ has been assumed. Dashed lines show $v^2 = 0$ and $v^2 = 9\sigma_r^2$.

2002). The object contains $N = 1\,190\,016$ dark matter particles, embedded in a $80 h^{-1}$ Mpc box in a Λ CDM universe ($\Omega_{\text{dm}} = 0.3$, $\Omega_\Lambda = 0.7$, $h = 0.7$). A thorough analysis of these numerical experiments can be found in Ascasibar et al. (2003, 2004).

A scatter plot of the real- and phase-space density of 2 per cent of the particles is shown in Fig. 16. Substructure gives rise to localized density peaks in both spaces, whereas most of the mass follows the global trend of decreasing density with radius. This component can be roughly described by a Hernquist model with $M = 3.6 \times 10^{14} M_\odot$ and $a = 250$ kpc, plotted as solid lines in the figure.

Satellite haloes achieve higher central densities than the main object, and the effect is more pronounced in phase-space. Therefore, the high end of the volume distribution $v(f)$ will be dominated by substructure. We plot this quantity in Fig. 17, together with the power-law behaviour advocated by Arad et al. (2004). Although our results are consistent with $v(f) \propto f^{-2.5}$ over 4 decades in f , we find departures from this law both at low and high phase-space densities. Similar results are reported by Arad et al. (2004), but deviations from a pure power law are attributed to a lack of resolution at high f and incomplete virialization at low

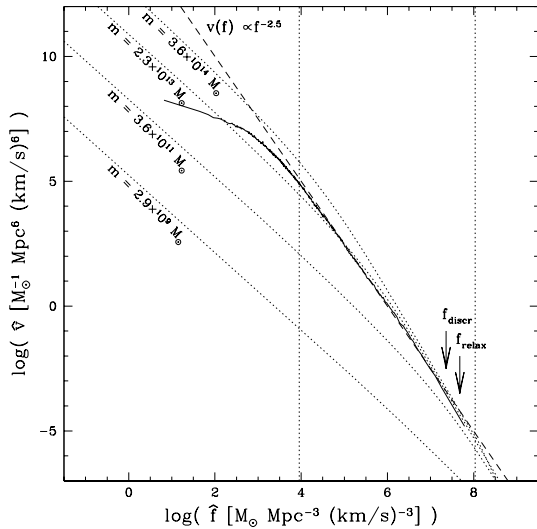


Figure 17. Volume distribution of phase-space density for a simulated halo (solid line). Dotted lines plot Hernquist models of different masses, while the dashed line shows $v(f) \propto f^{-2.5}$. Vertical lines mark the expected turnovers in $v(f)$, and arrows the resolution limits of this simulation (see text).

f . We show below that such deviations are indeed expected theoretically for systems in virial equilibrium.

Also shown in Fig. 17 are the volume distributions of several Hernquist models with different masses. We use the same ‘concentration’ $c \equiv r_{200}/r_s = 8$ for all of them, where r_{200} is the radius at which the enclosed density is 200 times the critical density and $r_s = a/2$ is the point at which the logarithmic slope of the density profile is equal to -2 . With this prescription, the mass and scale length are related by

$$m = \frac{4\pi}{3} 200\rho_c \frac{c}{2} \left(\frac{c}{2} + 1\right)^2 a^3. \quad (19)$$

Note that the volume distribution of the Hernquist model tends asymptotically to $v(f \rightarrow 0) \propto f^{-1.56}$ and $v(f \rightarrow \infty) \propto f^{-2.8}$. The turning point occurs roughly at

$$f \sim 3.25 \times 10^{18} \left(\frac{m}{M_\odot}\right)^{-1} M_\odot \text{Mpc}^{-3} (\text{km s}^{-1})^{-3} \quad (20)$$

and

$$v \sim 5.46 \times 10^{-38} \left(\frac{m}{M_\odot}\right)^3 M_\odot^{-1} \text{Mpc}^6 (\text{km s}^{-1})^6, \quad (21)$$

where m is the mass of the halo.

In the toy model proposed by Arad et al. (2004), the total volume distribution is given by the convolution

$$v(f) = \int_0^\infty v_m(f) \frac{dn(m)}{dm} dm \quad (22)$$

of the individual $v_m(f)$ of each sub-halo with the sub-halo mass function $dn/dm \propto m^{-1.9}$ (De Lucia et al. 2004). It is important, though, that the mass m of the satellites cannot reach an arbitrary value. On one hand, the resolution of the simulation imposes a minimum mass $m_{\min} \sim 100m_p$. On the other hand, there is the physical constraint that m must be smaller than the mass of the main object.

Let us define

$$\phi \equiv \frac{f}{3.25 \times 10^{18} M_\odot^2 \text{Mpc}^{-3} (\text{km s}^{-1})^{-3}} \quad (23)$$

and approximate $v_m(f)$ as a double power law

$$v_m(f) \simeq \begin{cases} 5.46 \times 10^{-38} m^3 (m\phi)^{-1.56} & \text{for } \phi \leq 1/m \\ 5.46 \times 10^{-38} m^3 (m\phi)^{-2.8} & \text{for } \phi \geq 1/m. \end{cases} \quad (24)$$

We can evaluate expression (22) as

$$\begin{aligned} v(f) &\propto \phi^{-1.56} \int_{m_{\min}}^{1/\phi} m^{-0.46} dm + \phi^{-2.8} \int_{1/\phi}^{m_{\max}} m^{-1.7} dm \\ &= 3.28 \phi^{-2.1} - \frac{m_{\min}^{0.54}}{0.54} \phi^{-1.56} - \frac{m_{\max}^{-0.7}}{0.7} \phi^{-2.8} \end{aligned} \quad (25)$$

for $m_{\min} < 1/\phi < m_{\max}$, and

$$v(f) \propto \phi^\lambda \int_{m_{\min}}^{m_{\max}} dm m^{1.1+\lambda} \quad (26)$$

with $\lambda = -1.56$ for $\phi < 1/m_{\max}$ and $\lambda = -2.8$ for $\phi > 1/m_{\min}$.

According to this model, the logarithmic slope of the total volume distribution would vary smoothly from -1.56 to -2.8 as ϕ goes from $1/m_{\max}$ to $1/m_{\min}$, the shape of $v(f)$ being controlled by the values of these parameters. A constant power law $v(f) \propto f^{-2.1}$ can only be obtained in the limit $m_{\min} \rightarrow 0$ and $m_{\max} \rightarrow \infty$.

The phase-space densities implied by $m_{\min} = 3 \times 10^{10} M_\odot$ and $m_{\max} = 3.6 \times 10^{14} M_\odot$ are illustrated as vertical dotted lines in Fig. 17. We find strong evidence of the turnover of $v(f)$ at the low end. The logarithmic slope measured by FIESTAS is flatter than -2.1 over several orders of magnitude, and it is close to -1.56 at the physical scale dictated by the main halo. At the high end, the effects of m_{\min} are (not surprisingly) very close to our resolution limit.

Dynamical discreteness effects place an upper limit on the phase-space density at which a given cosmological simulation is trustworthy. These effects include those of granularity when the first non-linear structures form (Binney 2004) and two-body relaxation (Diemand et al. 2004).

The phase-space density above which the two-body relaxation time is shorter than the age of the universe is

$$f_{\text{relax}} \simeq \frac{0.34}{(2\pi)^{3/2} G^2 \ln \Lambda} \frac{1}{m_p t_0}. \quad (27)$$

For the simulation studied here, $m_p = 3 \times 10^8 M_\odot$ and $t_0 = 13$ Gyr. Substituting $\ln \Lambda \sim 6$,

$$f_{\text{relax}} = 4.8 \times 10^7 M_\odot \text{Mpc}^{-3} (\text{km s}^{-1})^{-3}. \quad (28)$$

The phase-space density at which the effects discussed by Binney become important is

$$f_{\text{discr}} \sim \frac{\eta m_p}{(H_0 \Delta q^2)^3} \leq \frac{(\Omega_m \rho_c)^2}{H_0^3 m_p} \quad (29)$$

where Δq is the comoving interparticle separation and η is a factor a little smaller than unity that depends on the precise time at which the first structures become non-linear. Therefore,

$$f_{\text{discr}} \sim 2.3 \times 10^7 M_\odot \text{Mpc}^{-3} (\text{km s}^{-1})^{-3}. \quad (30)$$

Both estimates yield similar values of the maximum phase-space density that can be reliably represented in an N-body simulation (for a detailed discussion, the reader is referred to Binney 2004). The steepening of the volume distribution at the resolution scale is a numerical artefact of the

simulation, not of our algorithm. The fact that it is detected and accurately measured suggests that smoothing and sampling errors in FIESTAS are significant only at the very large values of f at which the underlying simulation is dominated by discreteness effects.

The situation at the low end is far more complicated. Although the simple model we have considered in this section offers an interesting insight on the problem, it does not yield a reliable prediction of the total volume distribution. The phase-space volumes occupied by the satellites may intersect amongst themselves, and they obviously do with the phase-space volume occupied by the main object. Therefore, the total $v(f)$ of the system is much less than the sum over the individual sub-haloes, as equation (22) assumes. The phase-space density $f_m(\mathbf{r}, \mathbf{v})$ is additive, but the volume distribution $v_m(f)$ is not.

Deriving the shape and normalisation of $v(f)$ would require knowledge of the exact distribution of haloes in phase space. Qualitatively, we expect that most satellites are located in the low- f regions of the main halo. The phase-space density will increase in these regions, most likely flattening $v(f)$ at the low end. Hence, logarithmic slopes even flatter than -1.56 would not be unexpected on physical grounds, although there are also many numerical effects that contribute in the same direction. Some of them arise from the N-body technique (e.g. the limited number of high-resolution particles) and some of them are associated with FIESTAS (e.g. systematic bias at low f). It is difficult to disentangle these numerical artefacts from the genuine effects of substructure. Although we cannot establish a definite value for the asymptotic behaviour of $v(f)$ as $f \rightarrow 0$, we do conclude that it is probably flatter than a substructureless Hernquist sphere, $v(f \rightarrow 0) \propto f^{-1.56}$.

5 PERFORMANCE

State-of-the-art N-body simulations currently yield halos with up to $N \sim 10^7$ particles. Recent observational archives achieve a similar number of objects. However, it seems likely that the typical number of points in future astrophysical datasets will increase by orders of magnitude during the coming years (see e.g. Szalay & Gray 2001). Therefore, computational efficiency has become a crucial issue in data analysis. A very accurate algorithm is completely useless if it cannot be run in a reasonable amount of time.

Fig. 18 shows, as a function of the number of points N , the time required to recover densities on a garden-variety laptop PC (1.7 GHz, 1 Gb RAM). The open symbols show the time required to estimate the real-space density, while the filled symbols are for recovery of the phase-space density. Our algorithm scales as $N \log(N)$, shown as dotted lines, for $N \geq 10^3$ particles. The offset between real and phase space estimators arises because the typical number of neighbours a particle has rises with dimensionality d roughly like 2^d .

It took FIESTAS 730s to recover f from a set of $N = 10^6$ particles, whereas Arad et al. (2004) report that about a week is required with a Delaunay tessellation. In fact the contrast in speed is even more dramatic than this comparison would suggest, since nearly all the measured time for FIESTAS is given to smoothing: for $N = 10^6$ the creation of the binary tree requires only ~ 4 s independent of

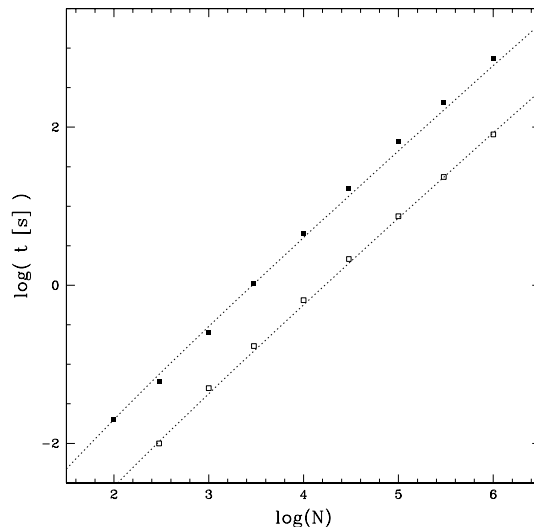


Figure 18. Computing time versus particle number for the recovery of real-space density (open symbols) and phase-space density (filled symbols). Dotted lines mark $N \log(N)$ scaling.

the number of dimensions. The density estimates of Arad et al. are unsmoothed ones and show the same large statistical fluctuations as our expression (2). Hence the week of computational time reported by Arad et al. ought strictly to be compared to the 4s it takes FIESTAS to produce unsmoothed density estimates.

6 CONCLUSIONS

In almost every branch of the physical, biological and social sciences one frequently wishes to determine the density of data points in some space. As all points in a given cluster are expected to have a common origin, identifying clusters through maxima in the density of points is likely to yield clues as to what processes are responsible for distributing points in the space. In the general case, each axis will represent a quantity with its own particular dimensions, and there is no natural definition of the distance between two data points.

The Field Estimator for Arbitrary Spaces (FIESTAS) that has been presented here provides a fast and accurate way of determining the density field underlying any given distribution of points. FIESTAS obtains a first estimate of the density by associating a volume with each data point and taking the density to be the inverse of that volume. Such an estimate inevitably fluctuates by of order 1 dex regardless of the number of data points, so it is desirable to smooth it. The computational cost of FIESTAS increases with the number of data points N as $N \log(N)$, and approximately as 2^d (probably $d \times 2^d$) with dimensionality d . For $d \lesssim 6$ and $N \lesssim 10^7$, smoothed densities within ~ 0.1 dex error bars (as long as the field is well sampled) are easily recovered on a single-processor computer.

The higher the dimension of the space within which densities are required, the greater is the fraction of the particles that lie near the boundary of the sampled volume. The determination of the density at the locations of these particles is problematical for any method because it depends

on what one takes to be the boundary of the sampled volume. We have experimented with various schemes for defining this boundary, without arriving at a definitive solution of the problem.

In tests with $d = 3$, we find that FiESTAS returns almost unbiased densities with 10^5 points in a Hernquist sphere. Statistical errors are ~ 0.1 dex over ten orders of magnitude in ρ . Smoothing tends to overestimate the density in low-density regions, while the opposite is true for the central, high-density region. Increasing the particle number extends the range of densities over which FiESTAS makes an unbiased estimate, but does not alter the magnitude of the statistical fluctuations in $\hat{\rho}$. Our tests show that density estimates obtained with the popular SPH kernel are significantly more strongly biased (towards large values) than are estimates from FiESTAS.

Most popular density estimators are not well suited to the evaluation of phase-space densities f because they require the distance between any two points to be defined and there is no natural definition of distance in phase space. Since FiESTAS does not involve the concept of distance, it is well suited to the estimation of f . A possible drawback of FiESTAS is its reliance on a coordinate grid, so density estimates will vary slightly when the grid is rotated. We confirm the results obtained by Arad et al. (2004) for a dark halo from a cosmological simulation, but at greatly reduced computational cost: the CPU time required is reduced from of order a week for raw densities to less than fifteen minutes for smoothed densities. This speedup makes feasible the determination of phase-space densities in simulations with up to 10^9 particles.

Although we confirm that over three to five decades in f the specific volume function follows a power law $v(f) \propto f^{-2.5}$, we find that at both the lowest and the highest phase-space densities, $v(f)$ falls below this power law, and we believe this phenomenon is not an artefact of our analysis. We are able to account for the form of $v(f)$ with a model in which a massive CDM halo is a superposition of a population of Hernquist profiles. A similar model was originally proposed by Arad et al., but in their analysis it did not reproduce $v(f)$ because they failed to recognize that in any given simulation there is both a smallest and a largest halo that can form.

The interest of FiESTAS extends far beyond the mere estimation of densities; it opens up a world of possibilities for both supervised and unsupervised classification. As an example of the latter, we are currently developing a halo finder in phase space. It has the advantage over conventional, real-space based methods that sub-haloes and tidal streams are very clearly defined in phase space that are not apparent in real space. Another possibility would be the identification of galaxy groups and clusters from observational data. Not being based on a particular metric, we expect FiESTAS to provide a robust parameter-free method that could exploit all the available information, such as coordinates on the sky, redshifts, colours, etc. Indeed, FiESTAS constitutes a general-purpose data-mining tool with many potential applications, not necessarily restricted to the field of Astrophysics.

ACKNOWLEDGMENTS

We thank I. Arad for a useful discussion and C. Nipoti for his comments on the manuscript. YA acknowledges support from the *Leverhume Trust* (United Kingdom).

REFERENCES

- Arad I., Dekel A., Klypin A., 2004, MNRAS, 353, 15
 Ascasibar Y., Yepes G., Gottlöber S., Müller V., 2004, MNRAS, 352, 1109
 Ascasibar Y., Yepes G., Müller V., Gottlöber S., 2003, MNRAS, 346, 731
 Bernardeau F., van de Weygaert R., 1996, MNRAS, 279, 693
 Binney J., 2004, MNRAS, 350, 939
 De Lucia G., Kauffmann G., Springel V., White S. D. M., Lanzoni B., Stoehr F., Tormen G., Yoshida N., 2004, MNRAS, 348, 333
 Diemand J., Moore B., Stadel J., Kazantzidis S., 2004, MNRAS, 348, 977
 Ebeling H., Wiedenmann G., 1993, Phys. Rev. E, 47, 704
 Gingold R. A., Monaghan J. J., 1977, MNRAS, 181, 375
 Helmi A., White S. D. M., 1999, MNRAS, 307, 495
 Helmi A., White S. D. M., Springel V., 2003, MNRAS, 339, 834
 Hernquist L., 1990, ApJ, 356, 359
 Hernquist L., Katz N., 1989, ApJS, 70, 419
 Kim R. S. J., Kepner J. V., Postman M., Strauss M. A., Bahcall N. A., Gunn J. E., Lupton R. H., Annis J., Nichol R. C., Castander F. J., Brinkmann J., Brunner R. J., Connolly A., Csabai I., Hindsley R. B., Ivezić Ž., Vogeley M. S., York D. G., 2002, AJ, 123, 20
 Knebe A., Green A., Binney J., 2001, MNRAS, 325, 845
 Kravtsov A. V., Klypin A. A., Khokhlov A. M., 1997, ApJS, 111, 73
 Lucy L. B., 1977, AJ, 82, 1013
 Marinoni C., Davis M., Newman J. A., Coil A. L., 2002, ApJ, 580, 122
 Monaghan J. J., 1992, ARA&A, 30, 543
 Moore B., Quinn T., Governato F., Stadel J., Lake G., 1999, MNRAS, 310, 1147
 Navarro J. F., Frenk C. S., White S. D. M., 1997, ApJ, 490, 493
 Okabe A., Boots B., Sugihara K., 1992, Spatial tessellations. Concepts and Applications of Voronoi diagrams. Wiley, New York
 Pelupessy F. I., Schaap W. E., van de Weygaert R., 2003, A&A, 403, 389
 Press W. H., Teukolsky S. A., Vetterling W. T., Flannery B. P., 1992, Numerical recipes in C. The art of scientific computing. Cambridge University Press, 2nd ed.
 Ramella M., Boschin W., Fadda D., Nonino M., 2001, A&A, 368, 776
 Richards G. T., Nichol R. C., Gray A. G., Brunner R. J., Lupton R. H., Berk D. E. V., Chong S. S., Weinstein M. A., Schneider D. P., Anderson S. F., Munn J. A., Harris H. C., Strauss M. A., Fan X., Gunn J. E., Ivezić Z., York D. G., Brinkmann J., 2004, ApJ, submitted ([astro-ph/0408505](#))
 Silverman B. W., 1986, Density Estimation for Statistics and Data Analysis. Chapman and Hall, 1986

Springel V., Hernquist L., 2002, MNRAS, 333, 649

Springel V., Yoshida N., White S. D. M., 2001, New Astronomy, 6, 79

Szalay A., Gray J., 2001, Science, 293, 2037